Met. Mater. Int., Vol. 23, No. 2 (2017), pp. 405~411
doi: 10.1007/s12540-017-6456-8

Large-Scale Room-Temperature Aqueous Synthesis of Co Superstructures with Controlled Morphology, and Their Application to Electromagnetic Wave Absorption

Rambabu Kuchi[1], Viet Dongquoc[1], Dojin Kim[1], Soon-Gil Yoon[1], Seung-Young Park[2], and Jong-Ryul Jeong[1,*]

[1]Department of Materials Science and Engineering, Graduate School of Energy Science and Technology, Chungnam National University, Daejeon 34134, Republic of Korea
[2]Department of Materials Science, Korea Basic Science Institute, Daejeon 34133, Republic of Korea

(received date: 4 July 2016 / accepted date: 26 August 2016)

In this work, we report on the large-scale room-temperature synthesis of Co superstructures using a facile liquid phase reduction method in an aqueous medium. This method yielded pure Co powders within a short period of time without the use of any surfactants. The morphological changes in the Co superstructures could be controlled simply by varying the amounts of reducing agent (hydrazine hydrate). The morphology of the Co powders systematically controlled from aggregated foliage to isolated microfoliage by increasing the hydrazine hydrate addition from 4 ml to 8 ml. The morphology-dependent electromagnetic properties, including the electric permittivity, and magnetic permeability, were investigated over the microwave frequency range, 2-18 GHz. Co isolated microfoliage showed a maximum reflection loss (RL) of -32 dB at 9 GHz with a matching thickness of 2.5 mm, whereas the aggregated foliage Co superstructures displayed a maximum RL of -17 dB at 11 GHz with a matching thickness of 2.5 mm. The stronger absorption for isolated microfoliage was ascribed to a continuous micro networks and vibrating microcurrent dissipation arise from size and shape of the isolated microfoliage. The calculated RL suggested that the as-prepared samples were potential microwave absorption candidates in the X-band region.

Keywords: Co superstructures, microfoliage, aggregated foliage, microwave absorption, magnetic loss, magnetic permeability

1. INTRODUCTION

The development of electromagnetic materials that absorb electromagnetic radiation has attracted significant attention with the recent increase in electromagnetic interference problems as a result of the rapid development of high-frequency circuit devices, electronic systems, and military application instruments that operate in the gigahertz (GHz) range [1,2]. Electromagnetic wave-absorbing materials have an ability to absorb electromagnetic energy and convert it into either thermal energy or other forms of energy through the cooperative action of electric, dielectric and magnetic loss [3]. On the basis of electromagnetic energy lost mechanism, the absorbing materials may be categorise in to three types: resistance, dielectric and magnetic loss materials. Practical applications demand that ideal electromagnetic wave-absorbing materials should provide the strong absorption, across a broad absorption bands, the material should be low in density, function in the thin layer form, and be low in cost [3].

*Corresponding author: jrjeong@cnu.ac.kr
©KIM and Springer

Towards the development of good electromagnetic wave absorbers, a variety of materials have been designed, synthesized, and investigated for their utility in microwave absorption. Such materials include graphene-Fe_3O_4 [4], $Li_{0.4}Mg_{0.6}Fe_2O_4$/TiO_2 nanocomposites [5], hierarchical Ni/SnO_2 nanocomposites [6], graphene@Fe_3O_4 @SiO_2@NiO nanosheets [7], and Co/C composites [8]. Studies of these materials have revealed that magnetic metallic materials are good candidate to increase magnetic loss and microwave absorption by incorporating into the composites. For example, metallic Co is one of the most important ferromagnetic material for microwave absorption because of its high saturation magnetization, high Curie temperature and uniformly dispersed in an insulator matrix [9-11]. Hence, to improve microwave absorption characteristics, many of the researchers have attempted to synthesize different Co morphologies since the morphologies of the magnetic materials are deeply influenced the permittivity and permeability. Such as the nanoplatelets [12], nano chains [13], hollow porous spheres [14], sponge like nanoporous structures [15], microflower like structures [16-19], hierarchical three-dimensional superstructures [20]. However, all of the processes developed above have need of complex precursors or surfactants, such

as cobalt acetate, glycols, potassium-sodium tartrate, polyvinyl-pyrrolidine (PVP), and sodium dodecyl benzene sulfonate. These processes require high temperatures, and long reaction times. The limitations of these processes not only increase the production costs, also introduce impurities and noticeably reduce the properties of the structures [21]. To the best of our knowledge, the previously reported Co materials were prepared at high temperature, long reaction times and use of surfactants. Also the reflection loss (RL) of the previous reports for the Co materials were not strong at the X-band region (8.2-12.4 GHz). Therefore, it would be valuable to develop a simple room-temperature method for the large-scale synthesis of pure-phase Co superstructures. Morphological control over the synthetic methods is necessary to further advance studies of the morphology-dependent electromagnetic properties of these materials and their microwave absorption characteristics at the X-band region.

In this study, we demonstrated a simple method for controlling the morphology of pure Co powders at room temperature using an aqueous phase reduction reaction without the need for surfactants and templates. The morphology-dependent electro-magnetic properties and the microwave absorption characteristics of the resulting Co superstructure materials were studied as a function of frequency. The calculated RL revealed that the prepared Co powders have potential application to use as microwave absorbers. We also investigated the mechanism underlying the morphology-dependent electromagnetic response and microwave absorption properties.

2. EXPERIMENTAL PROCEDURE

All chemicals used in this process were commercially available in analytical grade purity and were used as received without further purification.

2.1. Synthesis procedure of co superstructures

The Co powders were prepared at room temperature in a 3-necked round bottom flask equipped with a magnetic stirrer. In a typical procedure, 40 ml of an aqueous solution were prepared by dissolving 1 g of $CoCl_2 \cdot 6H_2O$, 0.2 g of citric acid monohydrate, and a specific amount of triethyleneglycol monobutyl ether (TREGBE) in deionized water under magnetic stirring. After an intensive stirring over 10 min, NaOH solution (10 ml, 5 M) was added to the above solution. Then 2-8 ml of hydrazine hydrate was added to the system under vigorous stirring respectively, and the color of the solution changed from pink to dark blue at once. After the reaction had proceeded at room temperature for 1 hour, the appearance of a large quantity of black precipitate indicated the completion of the reaction. The precipitate was separated from the solution by puting a permanent strong magnet under the reaction flask and washing with deionized water and then absolute ethanol three times each. The resulted Co powders were obtained by vacuum drying of the wet precipitate at 40 °C for 24 h.

2.2. Characterization

X-ray powder diffraction (XRD) data were collected over the 2θ range of 30-80° by using a Bruker AXS D8 advanced diffractometer with a Cu Kα radiation source (40 kV and 40 mA) with Linxeye 1-D detector, a divergence angle of 0.2°, a step size of 0.02°, and an acquisition time of 0.5 s per step. The surface morphology of the prepared Co powders was observed using a field emission scanning electron microscope (FESEM, Hitachi, S-4800). The field dependent magnetization (M-H) curves at room temperature were measured using a vibrating sample magnetometer (VSM, Lakeshore 7304). The electromagnetic wave absorption properties of the Co powders with different morphologies were studied using a network analyzer (Agilent N5245A) over the frequency range 2-18 GHz. The cylindrical toroidal samples (with an outer diameter of 6.95 mm and an inner diameter of 3.05 mm) used for the electromagnetic measurements were prepared by homogeneously blending the Co powders with paraffin wax. Based on the Nicolson-Ross-Weir theory, the relative permittivity and permeability were determined using the T/R coaxial line method.

3. RESULTS AND DISCUSSION

For the synthesis of Co powders at room temperature, firstly the metal hydroxides ($Co(OH)_2$) were obtained by the addition of citric acid monohydrate to the precursor via the formation of metal citrate complex. The higher concentration (0.5 g) of citric acid results the fused structures as shown in Fig. 1(a). The formed metal hydroxides get hydrolyzed and release of Co^{2+} from the addition of NaOH. Finally by the addition of TREGBE, hydrazine hydrate led to the precipitate out the Co. The basic condition favors the anisotropic growth, but too much of base concentration adversely affected and the

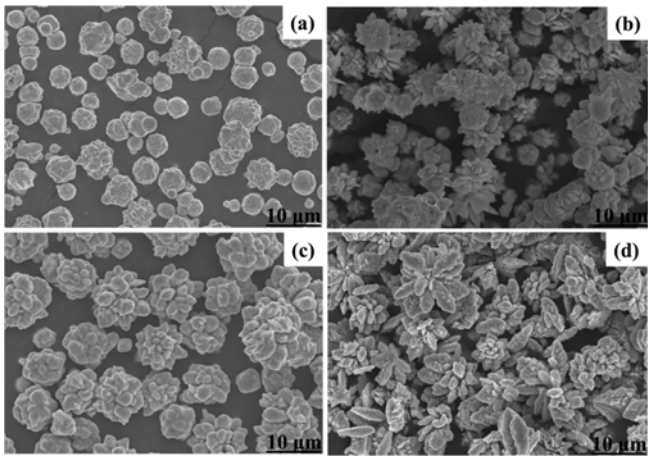

Fig. 1. SEM images of the Co powders prepared with excess (a) citric acid (b) NaOH (c) without the directing agent TREGBE (d) excess amount of TREGBE.

formation of unshaped structures was observed as shown in Fig. 1(b). Excessive amounts of NaOH reduced the release of Co^{2+} from $Co(OH)_2$ and leading to the thermodynamic change of nucleation and growth velocities [16]. The role of TREGBE in the reaction was investigated by preparing a sample without adding and with high amount of TREGBE holding all other parameters constant. In the absence of TREGBE, only an unshaped structures were obtained as shown in Fig. 1(c) and in the case of high amount of TREGBE there is a formation of some mixed structures shown in Fig. 1(d). Therefore, TREGBE plays an important role as structure director in obtaining the preferential oriented growth through the heterogeneous nucleation sites which could be obtained by the interaction between TREGBE molecules and Co particles via Vander Waals forces, surface defects and active crystal surface generation on early Co nuclei [16,22]. These Co nuclei can generate a magnetic field that promotes the arrangements of newly reduced atoms along the magnetic force lines [23].

Figure 2 shows the morphologies of as prepared products with varying amounts of hydrazine hydrate additions. Figure 2(a) indicates that the product obtained by the addition of 2 ml hydrazine hydrate consisted of a large number of big spheres composed of many small spheres. The addition of 3 ml hydrazine hydrate, produced a nearly aggregated foliage-like structure as shown in Fig. 2(b). From the Fig. 2(c, d) revealed that the addition of 4 ml hydrazine hydrate produced a sample possessed only of well-assembled three-dimensional (3D) aggregated foliage like Co superstructures which are made by ensembles of foliage petals. Increasing the amount of hydrazine hydrate to 6 ml, as shown in Fig. 2(e, f) yielded a product with an enlarged aggregated foliage-like structure along with some foliage petals. Further increasing the hydrazine hydrate to 8 ml, yielded only isolated microfoliage Co superstructures, because of oriented attachment and self-assembly of spherical cobalt grains.

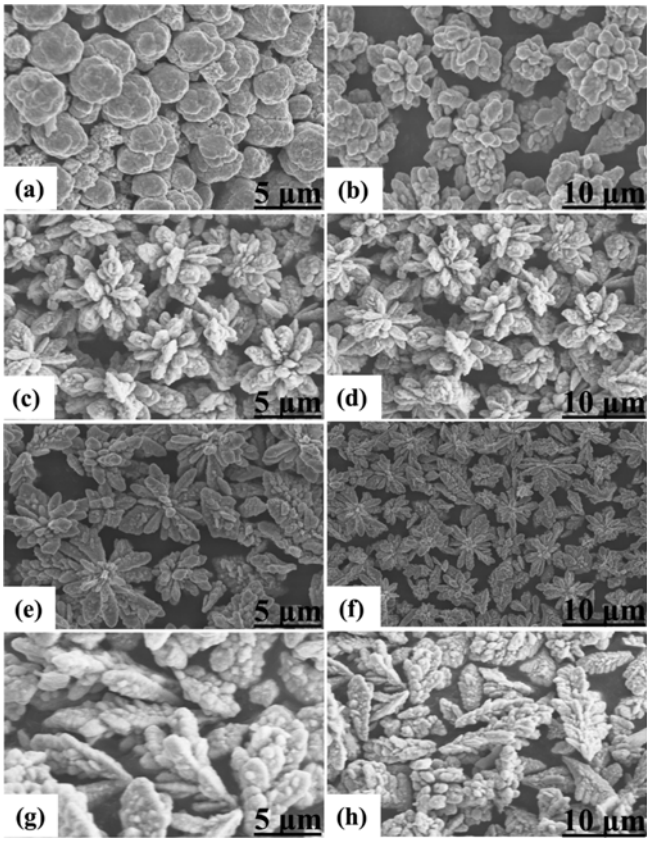

Fig. 2. SEM images of the Co superstructures synthesized using various amounts of hydrazine hydrate (98%). (a) Big sphere composed of small spheres, obtained using 2 ml hydrazine hydrate; (b) nearly aggregated foliage, 3 ml; (c, d) aggregated foliage like, 4 ml; (e, f) enlarged aggregated foliage, 6 ml; (g, h) isolated microfoliage, 8 ml.

The above results clearly indicated that aggregated foliage and isolated microfoliage superstructures formed by the addition of 4, 8 ml hydrazine hydrate and whereas in other conditions some intermediate structures were obtained. The formation mechanism of Co superstructures is possible to investigate on the basis of above results. It is reported that the morphology and size of Co crystals are dependent on the competition between nucleation and growth that can be altered by controlling the reaction rate [24,25]. The kinetics of nucleation and growth of reduced Co atoms may be well governed by varying amounts of hydrazine hydrate. The fractal growth of the aggregated foliage is normally linked with the diffusion-limited aggregation (DLA) and nucleation-limited aggregation (NLA) processes [16]. Oscillations in the metal ion concentrations during the violent stirring provide another influential factor to get the stable fractal formation and important for fractal growth and side branching phenomenon [26]. With the high concentration of hydrazine hydrate, the rate of reaction is faster, the system is not in equilibrium, and the promotion of DLA [27]. These conditions favor the formation of aggregated microfoliage Co superstructures. With further higher concentration of hydrazine hydrate, increases the reaction system energy and this additional energy served to get the isolated microfoliage through the cleavage of the side branches in aggregated foliage structure.

Figure 3(a) shows the XRD patterns of the Co superstructures prepared with different amounts of hydrazine hydrate. The diffraction peaks of the samples observed at $2\theta = 41.64°$, 44.49°, 47.28°, and 76.03° can be well-assigned to the (100), (002), (101) and (110) planes of the hexagonal phase Co (JCPDS 05-0727). There are no distinctive peaks are detected for the impure phases, such as Co oxides or hydroxides, revealed that the as synthesized products are pure hexagonal-close-packed (hcp) Co by our simple aqueous strategy at room temperature. Especially, the relative intensities of the peaks corresponding to the (002)/(100) planes is 3.2 (standard value is 3.0) and (002)/(101) planes is 0.63 (standard value is 0.6) for isolated microfoliage. For the other structures are also have cosiderably higher values than the standard values. These results suggested that the growth was not dependent on the morphology and it

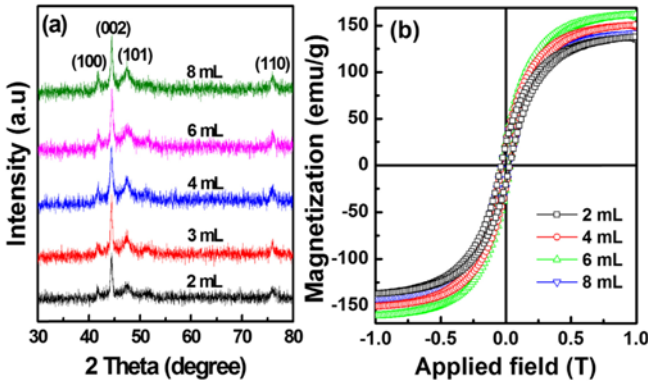

Fig. 3. (a) X-ray diffraction patterns (b) Magnetization curves of the Co superstructures prepared with different volumes of hydrazine hydrate.

was orientated preferentially along the [001]. Figure 3(b) represents the magnetization hysteresis curves of Co superstructures at room temperature. Among the all samples, 2 ml sample have the minimum saturation magnetization value of 134.6 emu/g, 6 ml sample have the maximum saturation magnetization value of 158.5 emu/g, respectively. The saturation magnetization for the aggregated foliage and isolated microfoliage structures was 147.11 emu/g and 139.69 emu/g, respectively. The different saturation magnetization values for these structures may attributed to the different crystallite size in their structures and it was checked from the mean crystallite sizes calculation from XRD data by using Scherrer formula. The mean crystallite sizes of aggregated foliage, isolated microfoliage structures are 15.3, 14.3 nm respectively. So, these results are shown that the magnetic properties of these structures are dependent on crystallite size. The coercivity of these two structures were 317.01 Oe and 323.46 Oe, respectively, and were higher values than that of bulk Co (10 Oe) [28]. The enhancement of coercivities were ascribed to the size dependent coercivity due to different magnetization process usually observed in fine magnetic particles.

It is well known that the real parts of permittivity, permeability are indicative of the electromagnetic energy storage capacity, and in the otherhand the imaginary parts correspond to the loss capacity. Figure 4 presents the frequency-dependent electromagnetic properties of the Co superstructures over the microwave frequencies 2-18 GHz. It can be seen that both the real parts of permitvity (ε') and permeability (μ') of aggregated foliage and isolated microfoliage Co decreased with increasing frequency, which favored the electromagnetic wave absorption due to the frequency dispersion effect. Figure 4(a) exhibits the variation of real and imaginary permittivity as a function of the frequency. The isolated microfoliage Co displayed larger real, imaginary parts compared to the aggregated foliage Co superstructures. Broad resonance peaks in real part permitivity centered at 9.24 GHz, 11.05 GHz for isolated microfoliage and aggregated foliage Co respectively. The imaginary parts of these samples exhibit absorption peaks that coincided

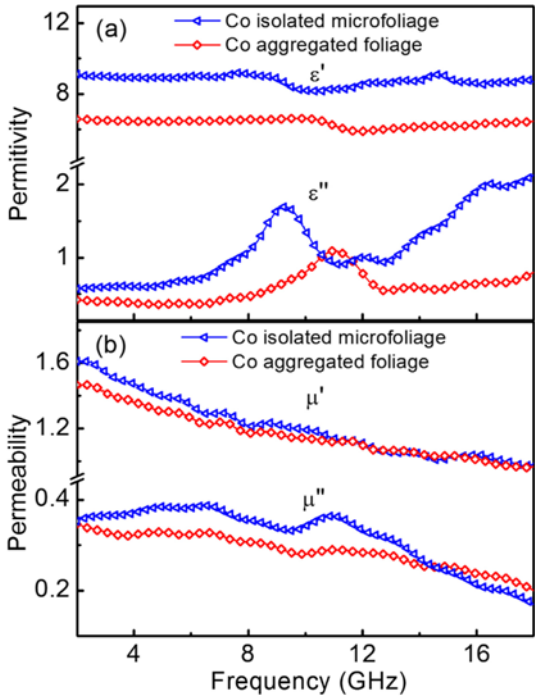

Fig. 4. Frequency-dependence of the electromagnetic properties of the Co superstructures with different morphologies (a) real part, imaginary part of complex permittivity (b) real part, imaginary part of complex permeability over the microwave range, 2-18 GHz.

with the resonance posotion in the real parts. Figure 4(b) shows the real and imaginary part of the permeability as a function of the frequency. The isolated microfoliage Co sample exhibited the higher imaginary part than the aggregated foliage Co.

Figure 5(a) show dielectric and magnetic losses of the Co superstructures. As we expected, it clearly shows that the magnetic loss is higher than dielectric loss. The maximum magnetic loss of aggregated foliage Co was 0.26 whereas for the isolated microfoliage Co superstructures the maximum magnetic loss value was 0.32. To verify the detailed mechanisms of the magnetic loss in the Co superstructures, we calculated the contribution of eddy current loss using the eddy current loss equation $\mu''(\mu')^{-2}f^{-1} = 2\pi\mu_o d^2\sigma$ [1,29]. Here μ_o is the vacuum permeability, μ' is the real part of permeability, μ'' is the imaginary part of permeability, σ is the conductivity, f is the microwave frequency and d is the thickness of the sample. According to the equation, if the magnetic loss results mainly from eddy current loss, the values of $\mu''(\mu')^{-2}f^{-1}$ should be constant over all frequencies. If not, the magnetic loss may be ascribed mainly to natural and exchange resonances. Figure 5(b) shows that the values of $\mu''(\mu')^{-2}f^{-1}$ for the Co superstructures decreased with increasing frequency. These results indicated that magnetic loss in the Co superstructures was mainly attributed to natural and exchange resonances. The first resonance peak at low frequency was ascribed to a natural ferromagnetic resonance that often appears at low frequency

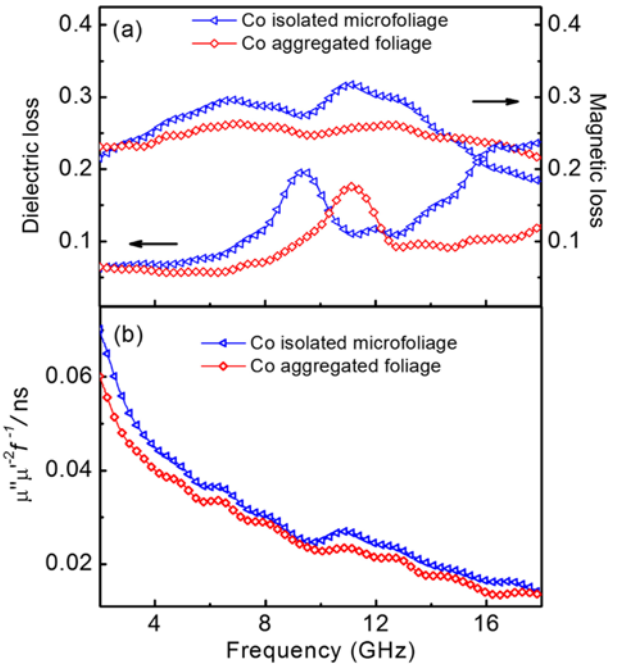

Fig. 5. (a) Frequency-dependence of dielectric, magnetic loss (b) $\mu''\mu'^{-2}f^{-1}$ of the Co superstructures with different morphologies over the microwave range, 2-18 GHz.

[12,30-33]. The second broad resonance peak at 10-15 GHz in our Co superstructures was attributed to an exchange resonance, consistent with the values reported for magnetic materials [12,34-40].

In the microwave transmission lines, the attenuation constant (α) and characteristic impedance (Z) are important parameters for determining reflection loss. The attenuation constant was calculated using the following equation [29].

$$\alpha = \left(\frac{\sqrt{2}\pi f}{c}\right)\sqrt{(\mu''\varepsilon'' - \mu'\varepsilon')} + \sqrt{(\mu''\varepsilon'' - \mu'\varepsilon')^2 + (\varepsilon'\mu'' - \varepsilon''\mu')^2} \quad (1)$$

where f is the microwave frequency and c is the velocity of light. Figure 6(a) plots the frequency dependence of the microwave attenuation in the Co superstructures. The high magnitude of the attenuation constant over the microwave frequency range of 2-18 GHz indicated the excellent microwave absorption in the prepared Co superstructures. The thickness dependence of the RL values was calculated and shown in Fig. 6(b,c). The RL was estimated from the permittivity ($\varepsilon_r = \varepsilon' - j\varepsilon''$) and permeability ($\mu_r = \mu' - j\mu''$) values according to the following equations [14,29].

$$RL = 20\log\left|(Z_{in} - Z_0)/(Z_{in} + Z_0)\right| \quad (2)$$

$$Z_{in} = Z_0\sqrt{\mu_r/\varepsilon_r}\tanh\{j(2\pi fd/c)\sqrt{\mu_r/\varepsilon_r}\} \quad (3)$$

Here Z_0 is the impedance of free space, and Z_{in} is the input

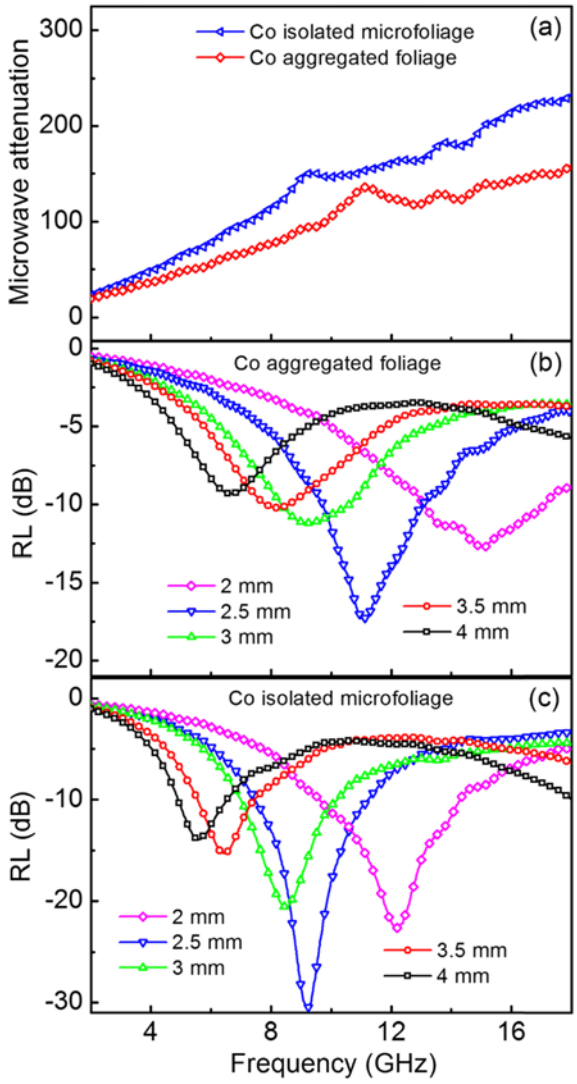

Fig. 6. (a) The microwave attenuation of the Co superstructures, (b) reflection loss (RL) for isolated foliage (c) reflection loss (RL) for aggregated foliage Co superstructures with different thicknesses over the microwave range, 2-18 GHz.

impedance of the absorber, c is the velocity of light and d is the thickness of the absorber. The matching frequency was inversely proportional to the thickness (d) [6], and this relation ship is given by the 1/4 wavelength equation $d_m = nc/4f_m(\sqrt{\mu_r/\varepsilon_r})$. The aggregated foliage Co provided a maximum RL of -17.76 at 11.14 GHz with a matching thickness of 2.5 mm. The effective absorption bandwidth was 3.52 GHz from 9.60-13.12 GHz (Fig. 6(b)). A maximum RL of -31.08 dB at 9.24 GHz was obtained for the isolated microfoliage Co with a matching thickness of 2.5 mm, and the effective absorption bandwidth (≤ -10 dB) was 3.80 GHz from 7.43-11.23 GHz as shown in Fig. 6(c). Note that the two Co superstructures exhibited a maximum RL covers the X-band region (8.2-12.4 GHz) and the energy loss arose significantly from magnetic loss than from dielectric loss. The isolated microfoliage Co

superstructures provided the highest magnetic loss with a high RL.

The superior electromagnetic-wave absorption for the isolated microfoliage Co superstructure than the aggregated foliage structure can be attributed to the morphology of the isolated microfoliage Co. The isolated microfoliage has connections between large number of compacted spherical Co grains could lead to the formation of continuous micro networks and vibrating micro current under the electromagnetic field [14]. Thus the isolated microfoliage structures can acts as quasi-antenna receivers and leads to enhancement of the penetration of electromagnetic waves into the absorber, resulting in strong absorption [3]. However, for the aggregated foliage structures the energy attenuation was small compared to the isolated microfoliage due to its shape and size. These results suggest that the electromagnetic-wave absorption capabilities of Co isolated microfoliage was higher than aggregated foliage and considerably influenced by the detail morphology of the prepared Co superstructures.

4. CONCLUSION

In conclusion, we succeeded in preparing the isolated microfoliage and aggregated foliage-like Co superstructures by varying the amount of reducing agent (hydrazine hydrate) added to the reaction flask. The synthesis proceeds on a large scale at room temperature using an aqueous reduction method. Pure hcp single phase crystal structure for the two types of Co morphologies was observed. The aggregation mechanism, the structure directing agent TREGBE and the magnetization along the direction of magnetic easy axis all contributed to the formation of the aggregated foliage and microfoliage morphologies. The isolated microfoliage Co superstructures provided higher values of *Hc* than the aggregated foliage superstructures and it was attributed to the shape anisotropy. The isolated microfoliage Co provided higher dielectric and magnetic losses than the aggregated foliage-like Co, ascribed to their different morphologies. Magnetic loss contributed significantly to the RL. The calculated RL indicated that the Co superstructures provided optimal microwave absorption. A maximum RL of -31.06 dB at 9.24 GHz with a matching thickness of 2.5 mm was obtained for the isolated microfoliage Co superstructures. The effective bandwidth (< -10 dB) with a RL is about 3.8 GHz for the isolated microfoliage Co and 3.5 GHz for aggregated foliage Co. The Co superstructures prepared through a simple aqueous route provided a strong RL, and a broad absorption band and showed promise for use as microwave absorption materials in the X-band region.

ACKNOWLEDGEMENTS

This work was supported by a grant from the National Research Foundation of Korea funded by the Korean government (2016R1A2B4012847, 2013R1A4A1069528). This research was also supported by the Pioneer Research Center Programthrough the National Research Foundation of Korea funded by the Ministry of Science, ICT and Future Planning (2011-0027908).

REFERENCES

1. H. Wua, L. Wang, and H. Wua, *Appl. Surf. Sci.* **290**, 388 (2014).
2. S. L. Wen, Y. Liu, X. C. Zhao, and J. W. Cheng, *J. Appl. Phys.* **116**, 054310 (2014).
3. B. Zhao, W. Zhao, G. Shao, B. Fan, and R. Zhang, *ACS Appl. Mater. Inter.* **7**, 12951 (2015).
4. C. Hu, Z. Mou, G. Lu, N. Chen, Z. Dong, L. Qu, *et al. Phys. Chem. Chem. Phys.* **15**, 13038 (2013).
5. P. Bhattacharya, G. Hatui, A. Mandal, C. Das, R. Kumar, and T. C. Shami, *J. Alloy. Compd*. **590**, 331 (2014).
6. B. Zhao, B. Fan, G. Shao, W. Zhao, and R. Zhang, *ACS Appl. Mater. Inter.* **7**, 18815 (2015).
7. L. Wang, Y. Huang, X. Sun, H. Huang, P. Liu, M. Zong, *et al. Nanoscale* **6**, 3157 (2014).
8. R. Qiang, Y. Du, D. Chen, W. Ma, H. Zhao, X. Han, *et al. J. Alloy. Compd.* **681**, 384 (2016).
9. L. Yan, J. Wang, X. Han, Y. Ren, Q. Liu, and F. Li, *Nanotechnology* **21**, 095708 (2010).
10. Y. Kang, M. Cao, J. Yuan, L. Zhang, B. Wen, and X. Fang, *J. Alloy. Compd.* **495**, 254 (2010).
11. B. Wang, J. Zhang, T. Wang, L. Qiao, and F. Li, *J. Alloy. Compd.* **567**, 21 (2013).
12. J. Li, J. Huang, Y. Qin, and F. Ma, *Mat. Sci. Eng. B* **138**, 199 (2007).
13. X.-L. Shi, M.-S. Cao, J. Yuan, and X.-Y. Fang, *Appl. Phys. Lett.* **95**, 163108 (2009).
14. C. He, S. Qiu, X. Wang, J. Liu, L. Luan, W. Liu, *et al. J. Mater. Chem.* **22**, 22160 (2012).
15. J. Kong, F. Wang, X. Wan, J. Liu, M. Itoh, and K. Machida, *Mater. Lett*. **78**, 69 (2012).
16. C. Wang, X. Han, X. Zhang, S. Hu, T. Zhang, P. Xu, *et al. J. Phys. Chem. C* **114**, 14826 (2010).
17. Z. Ma, Q. Liu, J. Yuan, Z. Wang, C. Cao, and J. Wang, *Phys. Status Solidi B* **249**, 575 (2012).
18. G. Tong, J. Yuan, W. Wu, Q. Hu, H. Qian, L. Li, *et al. Cryst. Eng. Comm.* **14**, 2071 (2012).
19. C. Wang, S. Hu, X. Han, W. Huang, and L. Tian, *PLoS One* **8**, e55928 (2013).
20. S. L. Wen, Y. Liu, and X. Zhao, *Adv. Powder Technol.* **26**, 1520 (2015).
21. J. Osuna, D. de Caro, C. Amiens, B. Chaudret, E. Snoeck, M. Respaud, *et al. J. Phys. Chem.* **100**, 14571 (1996).
22. Y. Li, J. Zhao, Y. Zhu, D. Ma, Y. Zhao, S. Hou, *et al. Colloids Surface. A* **356**, 156 (2010).
23. J. Ye, Q. W. Chen, H. P. Qi, and N. Tao, *Cryst. Growth Des.* **8**, 2464 (2008).

24. P. Chai, X. Liu, Z. Wang, M. Lu, X. Cao, and J. Meng, *Cryst. Growth Des.* **7**, 2568 (2007).
25. X. H. Liu, R. Yi, Y. T. Wang, G. Z. Qiu, N. Zhang, and X. G. Li, *J. Phys. Chem. C* **111**, 163 (2007).
26. G. Zou, K. Xiong, C. Jiang, H. Li, T. Li, Y. Qian, *et al. J. Phys. Chem. B* **109**, 18356 (2005).
27. X. Zheng, L. Zhu, A. Yan, X. Wang, and Y. Xie, *J. Colloid Interf. Sci*. **268**, 357 (2003).
28. Y. L. Li, J. Z. Zhao, X. D. Su, Y. C. Zhu, Y. Wang, L. Q. Tang, and Z. C. Wang, *Colloids Surface. A* **336**, 41 (2009).
29. F. Wen, F. Zhang, and Z. Liu, *J. Phys. Chem. C* **115**, 14025 (2011).
30. F. Ma, Y. Qin, F. Wang, and D. Xue, *Scripta Mater.* **63**, 1145 (2010).
31. C. Kittel, *Phys. Rev.* **73**, 155 (1948)
32. R. Ramprasad, P. Zurcher, M. Petras, M. Miller, and P. Renaud, *J. Appl. Phys*. **96**, 519 (2004).
33. K. Rozanov, Z. Li, L. Chen, and M. Koledintseva, *J. Appl. Phys*. **97**, 013905 (2005).
34. A. Aharoni, *J. Appl. Phys*. **69**, 7762 (1991).
35. Y. Yang, C. Xu, Y. Xia, T. Wang, and F. Li, *J. Alloy. Compd*. **493**, 549 (2010).
36. L. J. Deng, P. H. Zhou, J. L. Xie, and L. Zhang, *J. Appl. Phys.* **101**, 103916 (2007).
37. D. Mercier, J.-C. S. Lévy, G. Viau, F. Fiévet-Vincent, F. Fiévet, P. Toneguzzo, *et al. Phys. Rev. B* **62**, 532 (2000).
38. S. M. Park, Y. M. Koo, B. Y. Shim, and D. N. Lee, *Met. Mater. Int*. **23**, 220 (2017).
39. J.-B. Ahn, D.S. Kim, S.-Y. Yoon, and C. J. Choi, *Korean J. Met. Mater.* **54**, 275 (2016).
40. J.-H. Kim and S.-S. Kim, *Korean J. Met. Mater.* **53**, 59 (2015).